Taylor & Francis
Taylor & Francis Group

Corrosion Engineering, Science and Technology
The International Journal of Corrosion Processes and Corrosion Control

ISSN: 1478-422X (Print) 1743-2782 (Online) Journal homepage: http://www.tandfonline.com/loi/ycst20

Helium effects on IASCC susceptibility in as-implanted solution annealed, cold-worked and post-implantation annealed 316L steel

I. Villacampa, J. C. Chen, P. Spätig, H. P. Seifert & F. Duval

To cite this article: I. Villacampa, J. C. Chen, P. Spätig, H. P. Seifert & F. Duval (2017) Helium effects on IASCC susceptibility in as-implanted solution annealed, cold-worked and post-implantation annealed 316L steel, Corrosion Engineering, Science and Technology, 52:8, 567-577, DOI: 10.1080/1478422X.2017.1323709

To link to this article: http://dx.doi.org/10.1080/1478422X.2017.1323709

Published online: 09 Oct 2017.

Submit your article to this journal

Article views: 42

View related articles

View Crossmark data

Full Terms & Conditions of access and use can be found at
http://www.tandfonline.com/action/journalInformation?journalCode=ycst20

Download by: [University of Michigan-Flint] **Date:** 23 October 2017, At: 09:31

CORROSION ENGINEERING, SCIENCE AND TECHNOLOGY, 2017
VOL. 52, NO. 8, 567–577
https://doi.org/10.1080/1478422X.2017.1323709

The Institute of Materials, Minerals and Mining
Taylor & Francis
Taylor & Francis Group

Helium effects on IASCC susceptibility in as-implanted solution annealed, cold-worked and post-implantation annealed 316L steel

I. Villacampa[a], J. C. Chen[a], P. Spätig[a], H. P. Seifert[a] and F. Duval[b]

[a]Department of Nuclear Energy and Safety, Paul Scherrer Institute, Villigen, Switzerland; [b]CEMHTI/CNRS, Université d'Orléans, Orléans, France

ABSTRACT

The susceptibility to irradiation-assisted stress corrosion cracking (IASCC) at relatively low dose is dominated by conventional mechanisms such as radiation-induced segregation, hardening, creep/relaxation and radiolysis. Large amount of helium (He) can be accumulated in reactor internal components made of nickel containing steels of pressurised water reactors after long-term operation. The increase of He content has been correlated to IASCC susceptibility in reactor internals subjected to neutron irradiation. However, the question whether He increases or even dominates the IASCC susceptibility at high doses is still open. In this work, He was homogeneously implanted at 300°C to 300 and 1000 appm. Slow strain rate tests were performed in as-implanted solution annealed and cold-worked samples and in post-implantation annealed samples. The results show that homogenised implanted He up to 1000 appm alone (without significant displacement damage) does not produce intergranular cracking and IASCC in high-temperature air and in hydrogenated high-temperature water, respectively.

ARTICLE HISTORY
Received 9 February 2017
Accepted 13 April 2017

KEYWORDS
316L steel; helium effects; cold work; solution annealed; post-implantation annealed; irradiation-assisted stress corrosion cracking; slow strain rate test; pressurised water reactor

Downloaded by [University of Michigan-Flint] at 09:31 23 October 2017

Introduction

Stress corrosion cracking (SCC) is the formation and subcritical growth of cracks in a material (usually in a susceptible condition) under the simultaneous and synergistic interaction of approximately constant mechanical tensile stress and corrosive environment. It only occurs for a critical combination of environmental, material and loading parameters. When irradiation is present, changes are produced in the microstructure and microchemistry of the material, in the environment, and in the stress–strain state leading to the SCC increase. In a nuclear reactor, where reactor internals are exposed to irradiation, stress and water environment, the most common failure mechanism is the so called (irradiation-assisted stress corrosion cracking) IASCC [1,2].

IASCC is caused by a synergy of different phenomena affecting the material (radiation-induced segregation and hardening, transmutation, radiation-enhanced diffusion, swelling, radiation-induced creep/relaxation and swelling) and the environment (radiolysis) that have been studied thoroughly for the last decades [3–6]. However, most of these studies have been devoted to clarifying the effect of radiation displacement damage on IASCC in terms of dislocation loops, voids, grain boundary segregation, hardening, precipitation and/or radiolysis mainly using material test reactors that irradiate materials with highly energetic neutrons [6–9].

Recent studies reveal that a significant amount of helium can be accumulated in nickel (Ni) containing pressurised water reactor (PWR) reactor internal components during long-term operation. The contribution of helium starts to be significant after several dpa (about 10–15 dpa) by Ni transmutation following the two-step reaction $^{58}\mathrm{Ni}(n;\gamma)^{59}\mathrm{Ni}(n;\alpha)^{56}\mathrm{Fe}$ caused by thermal neutrons [10]. The aging and the lifespan increase of the current nuclear reactor fleet open the door to highly concentrated helium reactor internals, especially those with high Ni content. This reflects a concern for an increased IASCC susceptibility and, in particular, for repair welding of highly irradiated internal components. The IASCC knowledge at high doses is mainly based on samples that were irradiated in material test reactors (fast neutrons) with much lower He production rates (0.2 appm/dpa) than in a PWR at late operation (10 appm/dpa). Therefore, this might significantly underestimate the real IASCC susceptibility at high doses for long-term PWR operation.

The IASCC susceptibility of austenitic stainless steels (AuSS) irradiated in a fast breeder reactor was much lower in slow strain rate tests (SSRT) in simulated PWR environment than that of AuSS irradiated in a PWR at the same high dose level, in spite of similar microstructures, hardening levels or grain boundary segregation [11]. The AuSS irradiated in the PWR revealed much higher He concentrations and the IASCC susceptibility correlated fairly well with the measured He contents. Therefore, it is suggested that the He might play an important role in IASCC of PWR core internals in addition to conventional mechanisms and that the mechanism at high irradiation doses could be different.

The He and irradiation effects are concomitant, which makes the quantification of their respective contribution to IASCC difficult. This study was undertaken to gain insight into the He effects on AuSS fracture mechanism, by implanting large amounts of He while keeping low displacement damage. So far, the helium studies were based either on material with non-homogeneous He concentration or on a protected environment (e.g. vacuum) or in thin samples that had a thickness of two to three times the grain size [12,13]. The uniqueness of this study is based on the He implantation temperature (relevant to light water reactors service temperature), the large implantation depth, the

CONTACT I. Villacampa ignasi.villacampa-roses@psi.ch Department of Nuclear Energy and Safety, Paul Scherrer Institute, CH-5232 Villigen, Switzerland

© 2017 Institute of Materials, Minerals and Mining Published by Taylor & Francis on behalf of the Institute

Downloaded by [University of Michigan-Flint] at 09:31 23 October 2017

Table 1. Composition of the nuclear grade 316L austenitic stainless steel used in this study (wt-%).

Fe	Ni	Cr	Mo	Mn	Si	Co	N	C	P	S
65	12.32	17.61	2.379	1.768	0.466	0.164	0.067	0.028	0.024	0.0029

homogeneous He distribution in the sample, the testing environment (relevant to PWR reactors) and the use of a miniaturised sample that represents the bulk properties of the material.

Experimental

Material, helium implantation and post-implantation annealing

The experimental material is a nuclear grade 316L AuSS with elemental composition given in Table 1. The material was solution annealed (SA) at 1050°C for 30 min and quenched in water. The microstructural study revealed an average grain size of 52 µm.

Tensile samples were manufactured in the SA and in the 20% cold-worked (CW) condition. They were electropolished after machining in order to remove any possible remaining surface hardening. The 20% CW material was produced by pre-deforming large tensile samples. Miniaturised tensile samples were then extracted from the gauge length of those large samples along the sample loading direction. The SA and CW microstructures are representative of the ones used in PWR baffle plates and baffle former bolts, respectively.

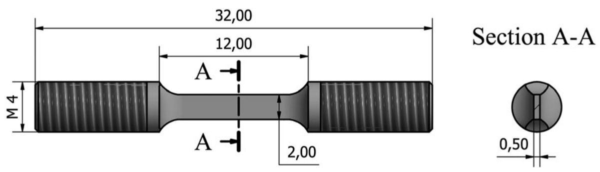

Figure 1. Miniaturised sample sketch. All dimensions are in mm.

Miniaturised samples with a thickness of 0.5 mm (~9× average grain size) were manufactured with the geometry presented in Figure 1. These revealed the same behaviour and tensile properties in air and high-temperature water as macroscopic standard samples as shown in a previous qualification study [14].

The He implantation was performed at the cyclotron of CEMHTI at CRNS Orléans from both sample sides with 45 MeV alpha particles at 300°C with a flux of 2.01 × 10^{13} He $cm^{-2}\,s^{-1}$ corresponding to a He implantation rate of 34.23 appm h^{-1} (Figure 2). An aluminium degrader with 24 different thicknesses is used for having a homogeneous He concentration through the gauge thickness (Figure 3). The helium to dpa ratio is 6250 appm He/dpa according to SRIM calculation in Kinchin–Pease (K–P) approach as suggested by Stoller et al. [15] (Figure 3).

SA and 20% CW samples were both implanted up to 1000 appm. The diameter of the He bubble size after implantation was below 1 nm and hence the helium bubbles could not be distinguished from dislocation loops. However, some of the SA samples were post-implantation annealed (PIA) from 750 to 1000°C for 1 h under high vacuum to vary the He bubble size, density and grain boundary coverage. This heat treatment increased the bubble size and reduced its density in the same way on the grain boundaries and in the matrix but no enhanced He accumulation on the grain boundaries was observed. The average bubble size increased from <1 nm in as-implanted condition to 29 nm in the matrix and 35 nm on the grain boundary for the highest annealing temperature (1000°C). The He bubbles average

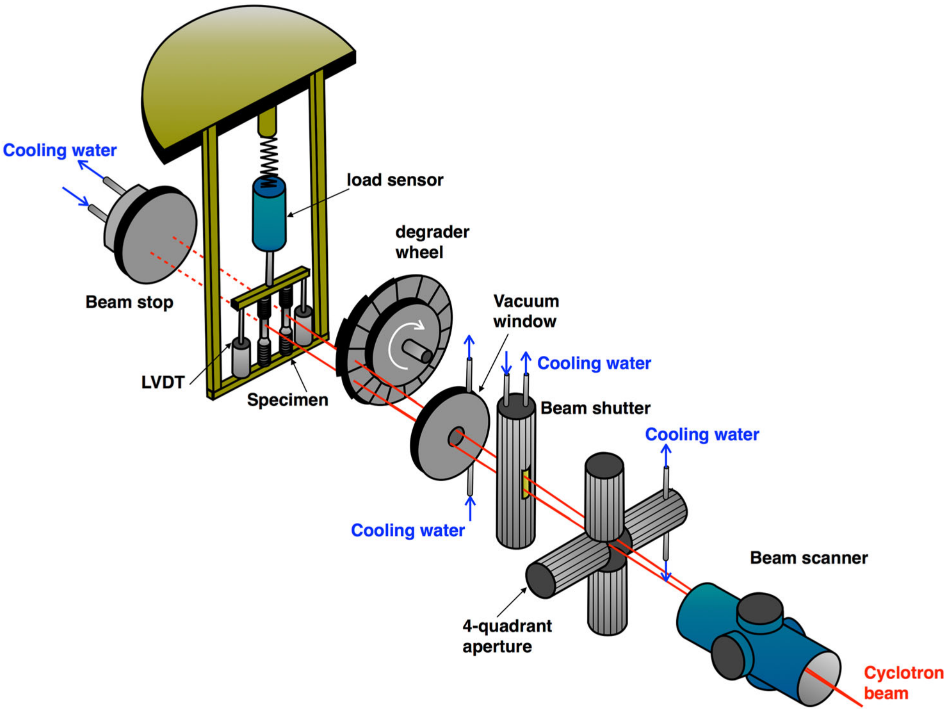

Figure 2. Schematic of He implantation facility.

Downloaded by [University of Michigan-Flint] at 09:31 23 October 2017

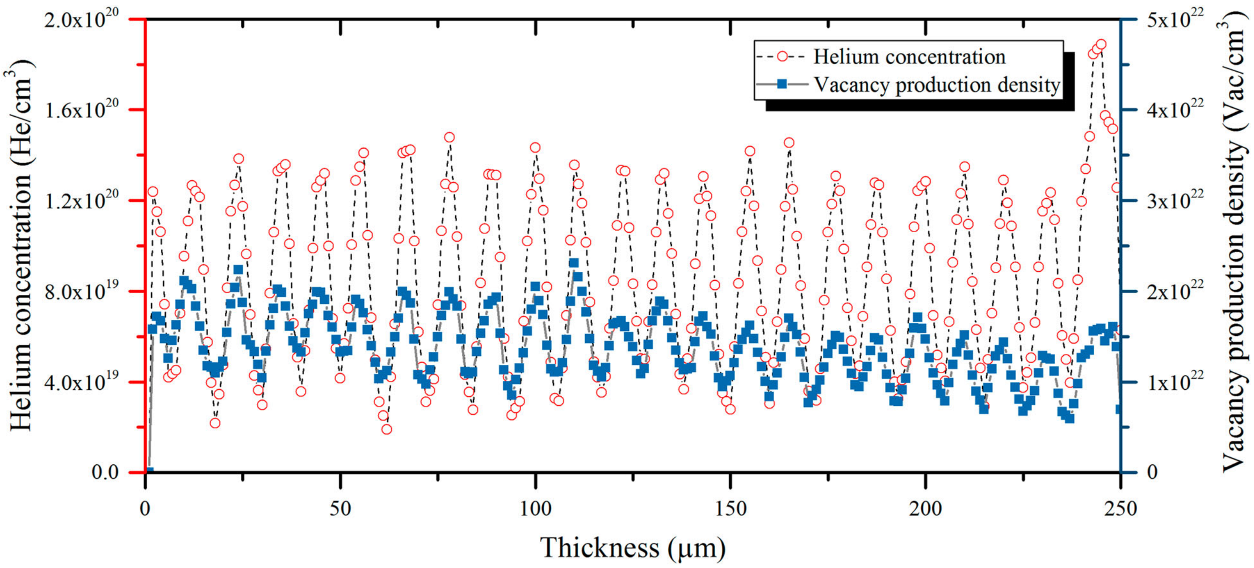

Figure 3. Helium and vacancy concentration profiles (along half sample thickness) calculated in Fe–12.32Ni–17.61Cr–2.379Mo–1.768Mn alloy with 45 MeV He ions to a fluence of 2.17 × 10^{18} He cm^{-2} using SRIM code in K–P approach with threshold displacement energy of 40 eV.

spacing on the grain boundaries and the grain boundary coverage increased from 11 to 139 nm and from 1 to 9% for the heat treatments from 650 to 1000 °C, respectively. The annealing at 750°C and at 850°C with 1000 appm gave similar He bubble average size and density than those observed in PWR baffle bolts [16]. The He concentration with 1000 appm corresponds to the operation of a mid-core baffle former bolt after long-term operation (~60 years) [17].

Slow strain rate testing

SSRTs were performed at a strain rate of 10^{-6} s^{-1} with the exception of one test which was performed at 10^{-7} s^{-1} in order to increase the exposure time to the environment. The strain rate of 10^{-6} s^{-1} was mainly selected as a reasonable compromise between susceptibility and number of possible tests due to time constraints. A lower strain rate usually further increases the susceptibility but then, restricts the number of investigated parameters and samples. Tests were carried out in two electro-mechanical tensile machines: one SSRT machine operating in high-temperature air (HTA); and a second tensile machine installed in an autoclave-water loop system (Figure 4, [18]) operating in hydrogenated neutral high-purity water (HTW) with 2.2 ppm of dissolved hydrogen at 288°C. The samples were kept 4 h in HTA and pre-oxidised for 5 days in HTW, before the SSRTs were started.

Post-test evaluations

The fracture, sample surface and fracture mode were investigated using scanning electron microscopy (SEM, 'NVision 40 FIB-SEM' with 15 kV) after the sample failure. The deformation microstructures were characterised by transmission electron microscopy (TEM, JEOL-2010 TEM. 200 kV). For this purpose, small disks of 3 mm were punched from the gauge length of the tested samples, which had been polished

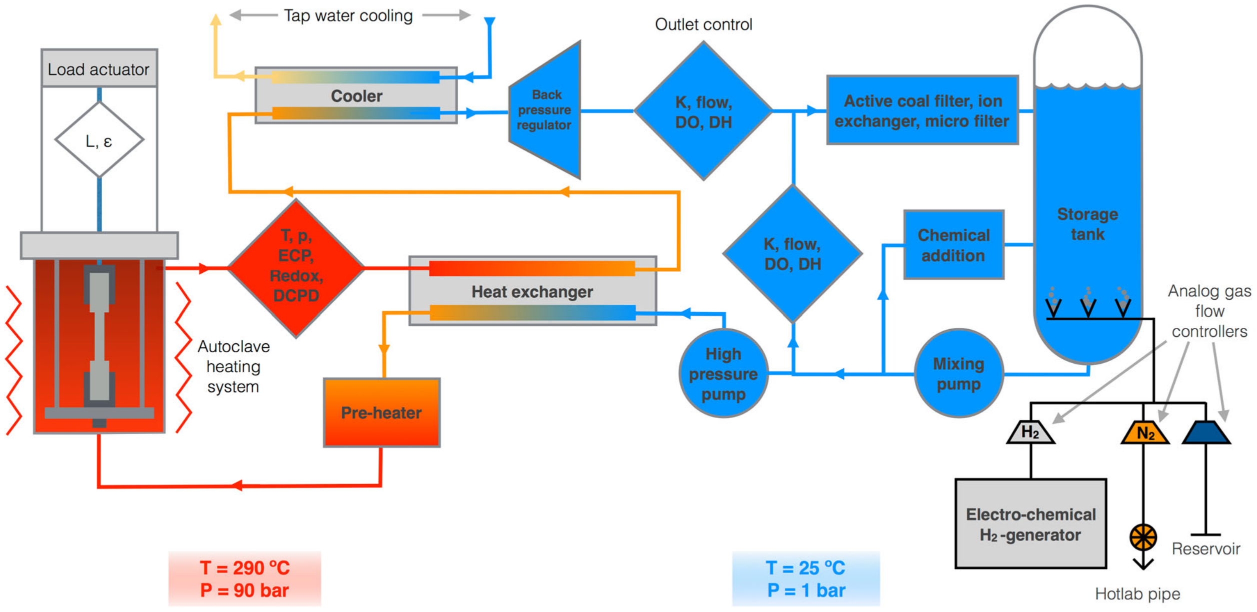

Figure 4. Schematic of the autoclave with the high-temperature water loop system.

Table 2. Summary of the engineering tensile test results.

Test conditions	He (appm)	Heat treatment	$Rp_{0.2\%}$ (MPa)	UTS (MPa)	US	RA	Fracture mode
SA-HTA $10^{-6}\,s^{-1}$	…	…	212	491	0.30	0.78	100% TG-D
SA-HTW $10^{-6}\,s^{-1}$	…	…	178	492	0.28	0.75	98% TG-D 2% TG-C
SA-HTW $10^{-6}\,s^{-1}$	300	…	273	532	0.30	0.67	99.8% TG-D 0.2% TG-C
SA-HTW $10^{-6}\,s^{-1}$	300	750°C-1 h	220	541	0.26	0.52	83.6% TG-D 17.4% TG-C
SA-HTW $10^{-6}\,s^{-1}$	300	850°C-1 h	212	533	0.26	0.78	100% TG-D
SA-HTW $10^{-6}\,s^{-1}$	300	950°C-1 h	209	530	0.27	0.53	88.8% TG-D 12.2% TG-C
SA-HTW $10^{-6}\,s^{-1}$	1000	…	418	594	0.26	0.67	99.3% TG-D 0.7% TG-C
SA-HTA $10^{-6}\,s^{-1}$	1000	…	383	547	0.23	0.76	100% TG-D
SA-HTW $10^{-6}\,s^{-1}$	1000	1000°C-1 h	198	512	0.27	0.48	98% TG-D 2% TG-C
CW-HTW $10^{-6}\,s^{-1}$	…	…	576	641	0.08	0.66	99.9% TG-D >0.1% TG-C
CW-HTA $10^{-6}\,s^{-1}$	…	…	515	590	0.08	0.79	100% TG-D
CW-HTW $10^{-6}\,s^{-1}$	1000	…	734	740	0.013	0.61	100% TG-D
CW-HTW $10^{-7}\,s^{-1}$	1000	…	787	790	0.001	0.54	97.5% TG-D 2.5% TG-C

TG-D: transgranular ductile fracture; TG-C: transgranular cleavage.

Downloaded by [University of Michigan-Flint] at 09:31 23 October 2017

down to 100 µm. Finally, these disks were electro-polished to perforation at −20°C with perchloric acid 5% and methanol 95% solution using Tenupol-5.

Results and discussion

SSRT

The tensile response and properties of the samples tested in HTA and HTW were very similar for a given material condition. The results are discussed hereafter and are summarised in Table 2.

decrease of yield stress at 288 C in water

Effect of HTW environment

In SA non-implanted samples, a remarkable softening with ~15% decrease of 0.2% yield stress ($Rp_{0.2\%}$) was consistently observed in the miniaturised samples, whereas the other tensile properties like ultimate tensile strength (UTS), uniform strain (US) or reduction of area (RA) were not affected (Table 2). The softening might be related to hydrogen absorbed from the environment and corrosion reactions and hydrogen-dislocation interactions (e.g. hydrogen-enhanced local plasticity (HELP)). Interestingly, this effect was not observed in standard samples [14]. At 288°C, the hydrogen diffusion distance during the pre-oxidation period is above the size of the used standard samples ($D \approx 6.29 \times 10^{-12}\ m^2\,s^{-1}$ from Kim et al. [19]), thus the hydrogen absorbed from the dissolved hydrogen in the environment cannot explain this difference. The crack depths observed in the samples were about 30 µm which means that the hydrogen was predominantly concentrated within the first µm of the sample. Therefore assuming the same absorption, the effect of hydrogen would be maximised in a thinner sample because the relative affected area would be greater. Thus, hydrogen has stronger effect on the overall plastic behaviour of the thin miniaturised sample than in thick standard sample.

Transgranular cleavage (TG-C) surface micro-cracks were observed along the whole gauge section, as described by Herms et al. [20], suggesting that they already initiated before the onset of necking (Figure 5). These micro-cracks were probably caused by hydrogen-assisted SCC and hydrogen embrittlement mechanism (adsorption induced dislocation-emission (AIDE), HELP or hydrogen-enhanced strain-induced vacancy (HESIV) embrittlement) as suggested by other authors [20–22]. There was no evidence of intergranular cracks in the fracture surface or in the sample surface since those cracks did not propagate smoothly. Further discussion is presented in the section ‘Fracture mode’.

The CW and He-implanted samples, on the other hand, showed a moderate hardening and increase of $Rp_{0.2\%}$ and UTS in HTW of about ~10%, but this observation is

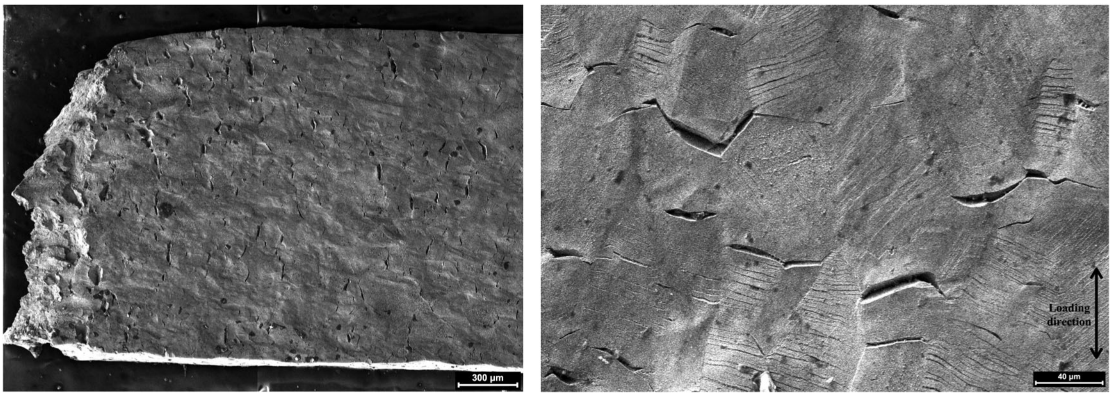

Figure 5. Transgranular cracks formed along the gauge length (left) and a close look to those cracks (image rotated 90°) far from the necking region (right) in a non-implanted SA sample tested in HTW.

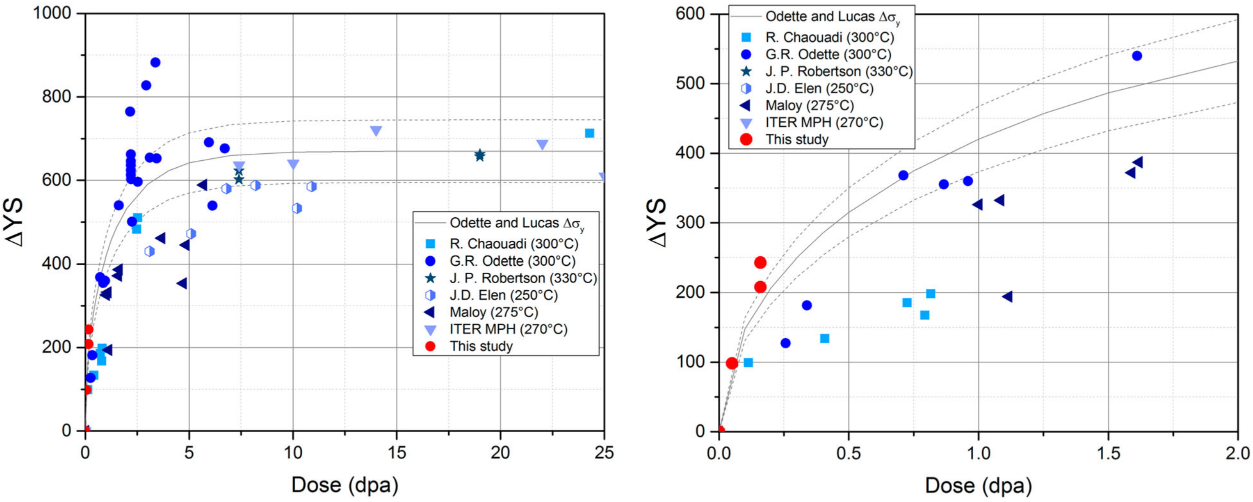

Figure 6. Comparison between the increase of YS with irradiation damage for tensile tests with He-implanted samples (300 and 1000 appm) in HTW and the Odette and Lucas equation w/o the error associated to the YS plateau (±75 MPa) [24] (left: full does range. right: zoom of low dose range). References: Chaouadi et al. [25], Odette and Lucas [24], Robertson et al. [26], Elen and Fenici [27], Maloy et al. [28] and ITER MPH from Chaouadi et al. [25].

Downloaded by [University of Michigan-Flint] at 09:31 23 October 2017

based on single samples only and might be rather related to the usual sample to sample scatter due to small local variations in CW and/or displacement damage from He implantation.

Most of the samples showed a shear fracture inclined 20–45° from the loading axis. This effect was reported, when hydrogen was present in the samples, both at low and high temperatures for different types of steels and for the standard samples analysed in a previous study [14,19,23], so it might be extrapolated to small sample thickness too.

The environment effect on the CW sample tested at lower strain rate (10^{-7} s^{1}) did not apparently modify the tensile properties or fracture surface (Table 2).

Effect of He implantation and post-implantation annealing

The He implantation resulted in a moderate but remarkable increase in $Rp_{0.2\%}$ and reduction in work hardening capacity (UTS – $Rp_{0.2\%}$) in as-implanted SA and CW samples at both, 300 appm (0.05 dpa) and 1000 appm (0.16 dpa) (Table 2). The hardening is comparable and consistent with other literature data of AuSS at the same level of displacement damage but without He thus, it seems primarily due to the displacement damage and not to the He bubbles (Figure 6). According to the results of Odette and Lucas [24], the irradiation hardening resulting from a mixed spectrum can mainly be attributed to displacement damage. Odette and Lucas proposed a correlation to estimate the YS in terms of neutron dose (dpa) in 300-series stainless steel irradiated and tested at about 300°C

$$\Delta\sigma_y = 670\ (\pm 75)\left[1 - \exp\left(-\frac{\text{dpa}}{2}\right)\right]^{0.5} \qquad (1)$$

The results of this work correlate fairly well with these data. The hardening after He implantation at 1000 appm is higher than the predicted by Odette and Lucas. This might be produced by the homogenously distributed He nano-bubbles in the grains which is estimated to be few tens of MPa and will be reported in a forthcoming publication.

In contrast to the $Rp_{0.2\%}$ and the UTS, the US was barely affected by He implantation in the SA materials (Figures 7 and 8). In CW materials, on the other hand, 1000 appm He implantation leads to drastic uniform elongation reduction, whereas the increase of $Rp_{0.2\%}$ and UTS was similar to the SA samples (Figure 9). The hardening induced by the CW

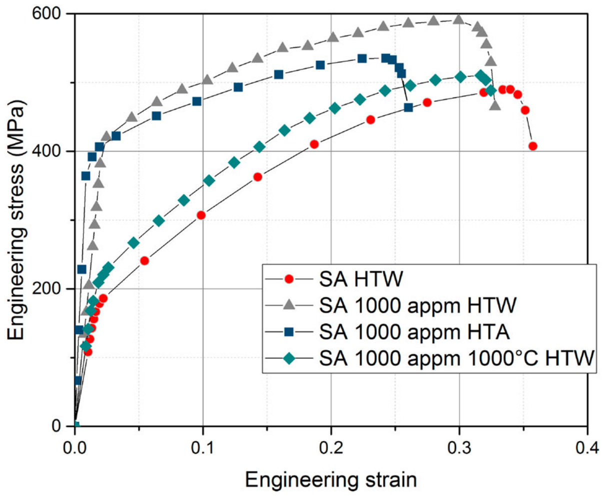

Figure 7. Engineering stress–strain curves in SA samples with/out 1000 appm He in HTW and in HTA. One implanted sample was annealed at 1000°C for 1 h (rhomboids symbols).

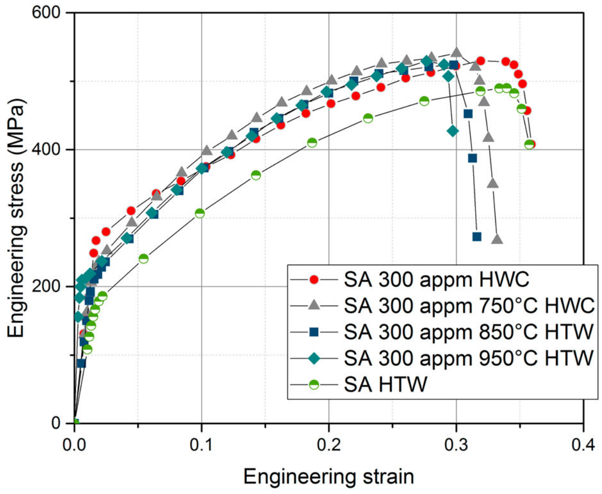

Figure 8. Engineering stress–strain curves in SA samples with/out 300 appm He in HTW. Three samples were annealed from 750 to 950°C.

Downloaded by [University of Michigan-Flint] at 09:31 23 October 2017

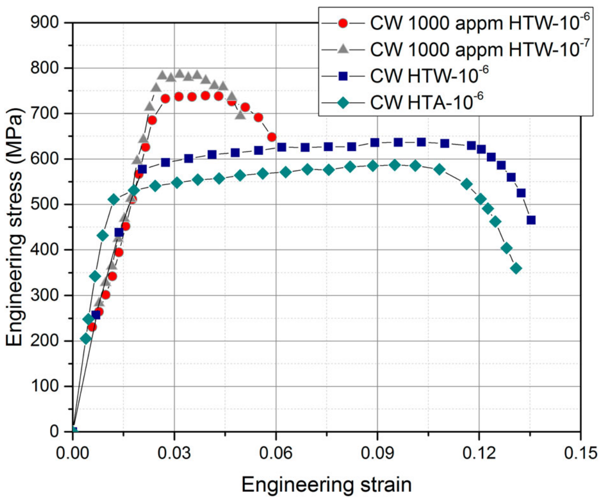

Figure 9. Engineering stress–strain curves of CW samples with/out 1000 appm He implantation tested in HTW and in HTA.

and the implantation at 1000 appm He shifted the $Rp_{0.2\%}$ to above 750 MPa. At this strength level, inter- and transgranular SCC may have higher chance to be observed in AuSS in hydrogenated HTW in pre-cracked samples. However, it is difficult to be reproduced in accelerated SSRT with smooth samples. Transgranular cleavage (TG-C) fracture was observed with full loss of macroscopic plastic deformation capacity in SSRT performed with smooth samples in vacuum at 25 and 300°C by Ullmaier and Chen [12], but both, displacement damage (≥1 dpa) and He contents (≥10 000 appm) where much higher than in this work.

Radiation damage and strain hardening capacity (UTS − $Rp_{0.2\%}$) are fully recovered by annealing at temperatures above 750°C (Figure 10). The remaining higher $Rp_{0.2\%}$ and UTS after annealing at different temperatures is quite similar among the materials with the same He concentration (Figure 10). This effect is produced by the He bubble hardening which depends on the bubble size and density (e.g. dispersed barrier hardening model [29,30]) that in turn depend on the implantation conditions (dose, dose rate and temperature), the He content and annealing temperature. The bubble size increases and the density decreases with increasing annealing temperature, resulting in a slight overall reduction of $Rp_{0.2\%}$ and UTS.

The dislocation loops and the nano-voids formed during the He implantation are presumed to be annealed after heat treatment above 750°C for 1 h. This is in line with Tsay et al. [31], where after a heat treatment above 650°C no black dots remained and only 10% of the as-implanted loop population was observed. According to the results of this study, the remaining hardening after annealing above 750°C is certainly due to the He bubbles. The bubble density decreases and the bubble size increases with higher annealing temperature. The larger bubbles are believed to act as harder obstacles, but this effect is overcompensated by the lower density and larger inter-bubble distance.

Fracture mode

The dominant fracture mode of all material conditions in both, air and hydrogenated high-temperature water, was transgranular ductile (TG-D) fracture by microvoid formation and coalescence (Figures 11–13). In HTW, minor and varying contributions of TG-C micro-cracks were detected starting at the water-wetted surface of the samples that ranged from 0 to 18% (Table 2; Figure 14). No intergranular cracking was observed so far. Thus, neither CW nor He implantation nor PIA significantly modified the failure process. The absence of intergranular cracking is probably due to little He enrichment on the grain boundaries as well as to the low probability of dislocation channelling occurrence for our samples. Indeed dislocation channelling comes into play for doses greater than about 0.1 dpa [32,33]. The grain boundary coverage after annealing is too low (<10%) to significantly reduce the grain boundary strength with respect to the matrix and, at the same time, the matrix hardening is completely annealed above 750°C which again prevents any localised deformation. This result is in line with Jiao et al. [34], where PIA reduced irradiation hardening and the degree of localised deformation. So far, intergranular cracking of single grain boundaries in micro-mechanical tests [35] and TG-C in polycrystalline materials [12] with He implantation were only observed at very high He contents with 20 000 and 10 000 appm He and higher irradiation damage (~1 dpa), respectively.

The TG-C surface micro-cracks always formed at the water-touched sample surface along deformation bands and were only present in HTW (Figures 5 and 15), but not in oxygenated water with 8 ppm O_2 [14]. They were observed along

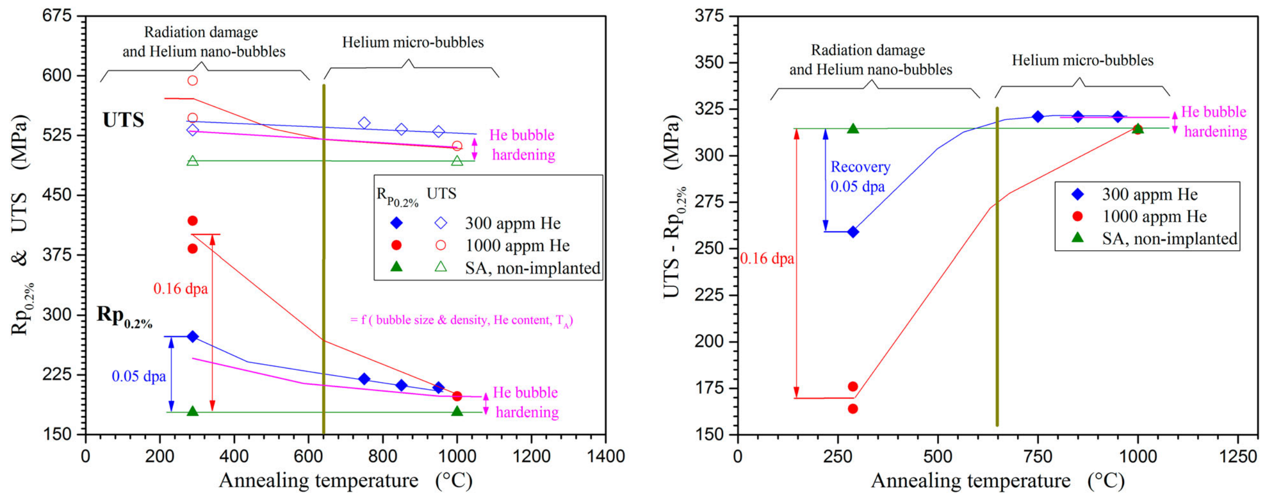

Figure 10. $Rp_{0.2\%}$ and UTS evolution (left) and strain hardening evolution (right) with increasing annealing temperature and varying He content.

Downloaded by [University of Michigan-Flint] at 09:31 23 October 2017

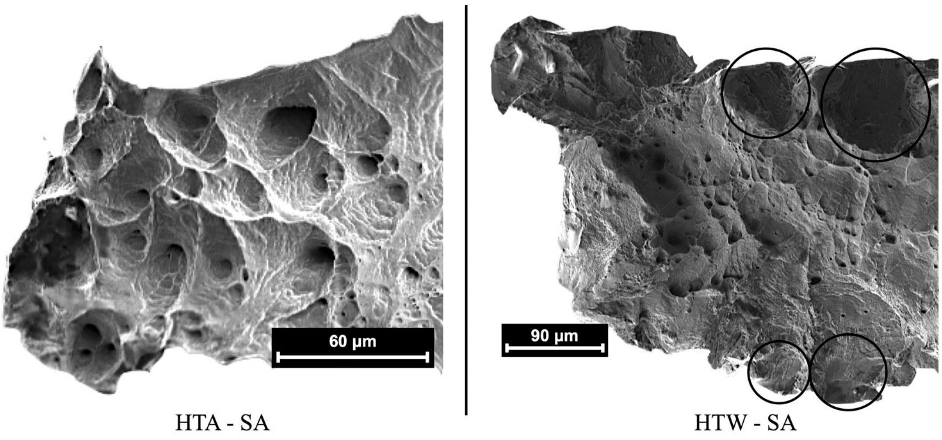

HTA - SA HTW - SA

Figure 11. Excerpt of fracture surface of the SA samples tested in HTA and HTW. Both samples showed dominant TG-D fracture with minor contributions to TG-C in HTW (black circles).

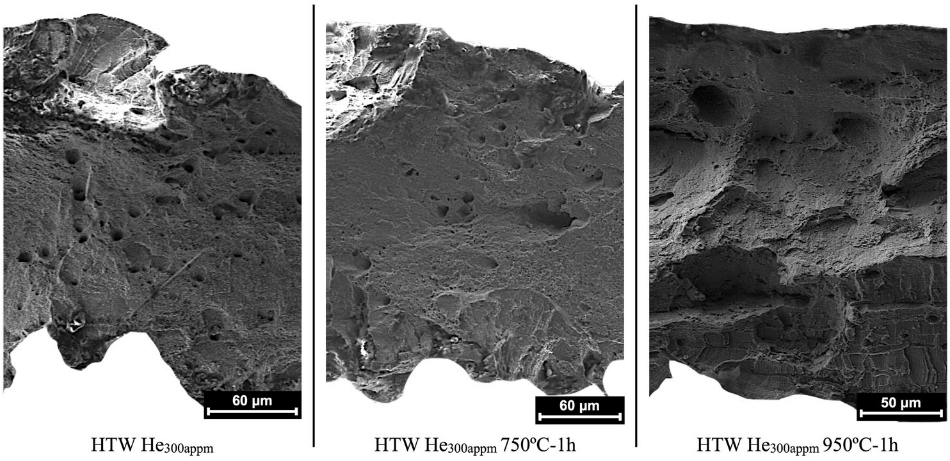

HTW He$_{300\text{appm}}$ HTW He$_{300\text{appm}}$ 750°C-1h HTW He$_{300\text{appm}}$ 950°C-1h

Figure 12. Excerpt of fracture surface of the samples tested with 300 appm. All the samples show dominant TG-D with minor contributions of TG-C in HTW.

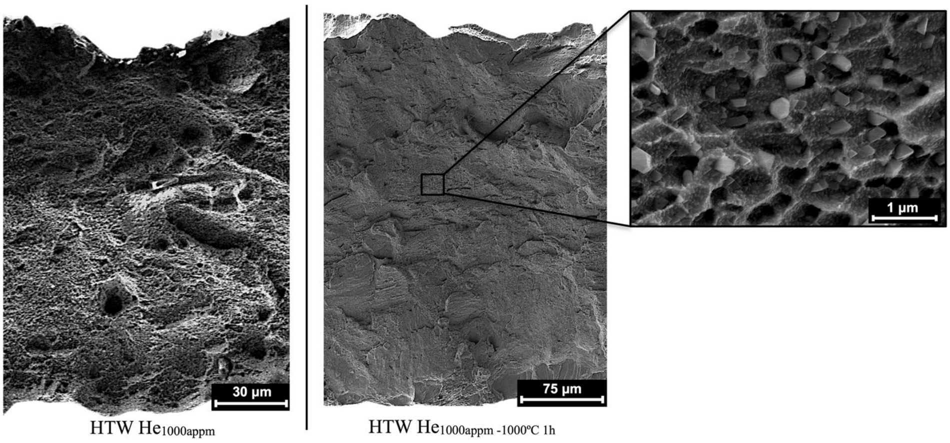

HTW He$_{1000\text{appm}}$ HTW He$_{1000\text{appm -1000°C 1h}}$

Figure 13. Excerpt of fracture surface of the samples tested with 1000 appm in HTW with/out PIA. A detail of the fracture surface is given for the heat-treated sample.

the whole gauge section, suggesting that they already initiated before the onset of necking. These surface cracks contained some striation-like features that seemed to be crack arrest markings from intermittent crack growth or slip steps (Figures 5 and 14). These cracks are thus environment-induced, probably due to hydrogen-assisted SCC and/or embrittlement mechanism (HELP or HESIV) [22]. At a first glance, the number of cracks and their openings were smaller and the surface crack length and crack depth shorter in the He-implanted samples, indicating that He bubbles could trap some of the available hydrogen from the environment and corrosion reactions reducing the degree of hydrogen embrittlement by various mechanisms. However, this effect should be studied more in detail.

Generally, the ductile dimples on the fracture surface formed in the centre of the samples are smaller in HTW

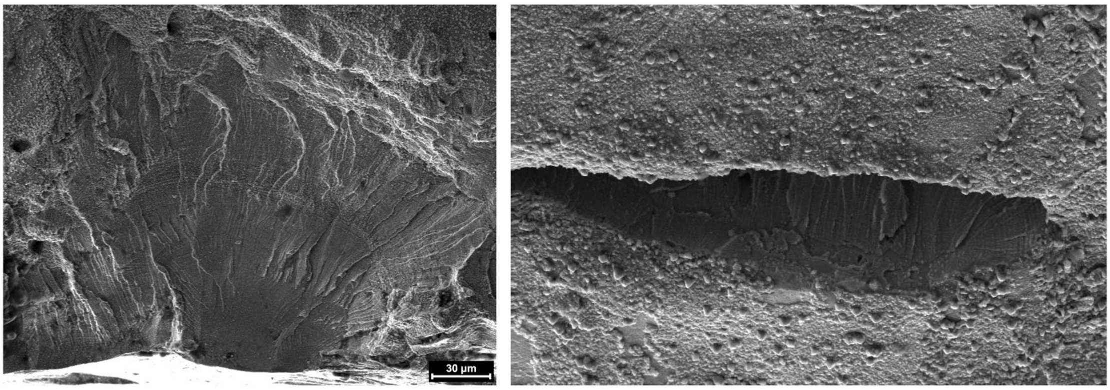

Figure 14. Typical TG-C crack formed in the fracture surface (left) and on the sample surface (right).

Downloaded by [University of Michigan-Flint] at 09:31 23 October 2017

than in HTA, indicating that hydrogen could play a role in reducing the void size (Figure 11). This effect has been also reported by Matsuo et al. [36]. Apart from the TG-C surface cracks, He implantation did not contribute to any particular change on the fracture surface with 300 appm in as-implanted and annealed (up to 950°C) conditions (Figure 12). The as-implanted He samples with 1000 appm tested in HTA and HTW showed a fracture surface similar to the as-implanted 300 appm (Figure 13) [37]. Therefore, the ductile dimple size was similar to non-implanted materials for the same environment. This suggests that the nucleation sites for microvoid formation and the subsequent growth and coalescence process are the same and He bubbles play a minor role in the ductile damage process here. However, the PIA carried out at 1000°C changed significantly the appearance of the fracture surface (Figure 13). The rupture appearance is microscopically ductile with a minor contribution of TG-C fracture (~2%), but almost free of larger macroscopic dimples. The average He bubble diameter in this condition is about 60 nm, which is not far from the dimple diameters observed. Large He bubbles seem thus to affect the ductile damage process.

Deformation microstructure

TEM investigations revealed slightly different deformation microstructures between SA/CW and as-implanted He samples (Figure 16). All the TEM samples were taken from the gauge length outside the necking region and were thus plastically strained up to the uniform strain (e.g. ~30% for SA non-implanted material). The sum of 20% CW and uniform strain for CW materials is similar to the SA ones. The CW materials with 1000 appm He had a highly deformed initial microstructure and hence, this made the differentiation of changes in deformation mechanism rather challenging.

SA and CW samples showed high dislocation density arranged in cell walls separated by relatively dislocation-free regions (Figure 16(A,B,G)). Deformation bands, both twins and slip bands can be observed (Figure 17). As-implanted SA samples showed also a high density of dislocations, but well developed dislocation arrangements were not identified (Figure 16(D,F)). Moreover, many black dots were observed in between the dislocation network, which could be irradiation defects (<1 nm) that act as obstacles for dislocation motion. As-implanted CW samples, on the other hand, showed a microstructure that resembled to that of SA samples, although the dislocation cells were generally less well defined (Figure 16(H)). The similar structure is not surprising, since, on one hand, dislocation cells were already formed during CW and on the other hand, a part of the irradiation damage or He might be absorbed by the forest dislocation network during implantation.

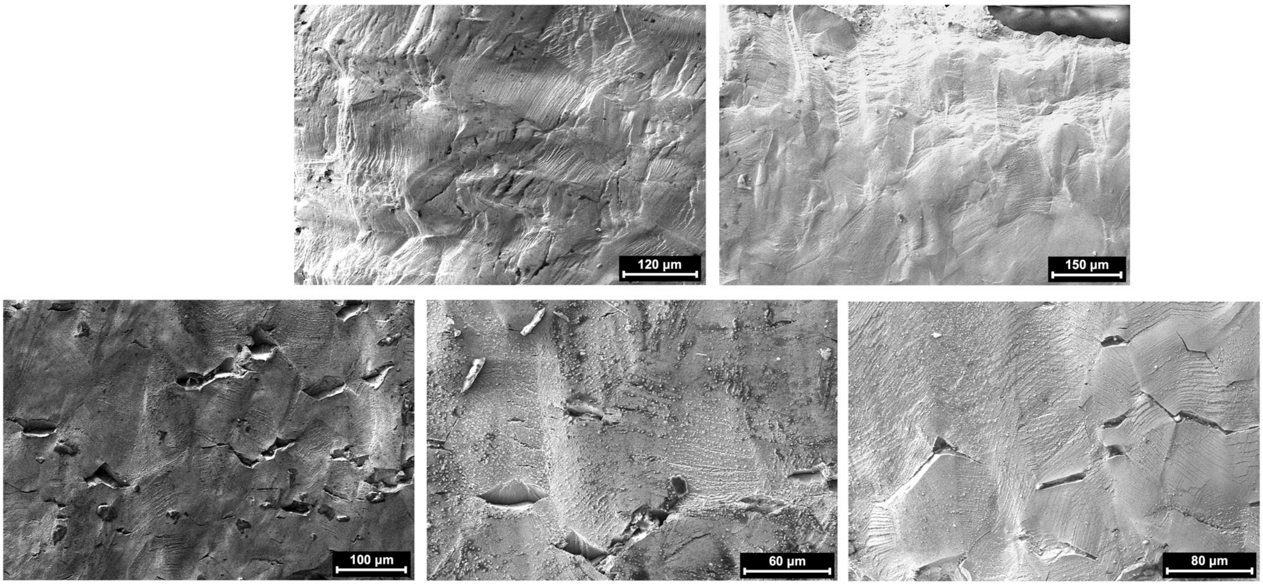

Figure 15. Sample surface detail of the samples tested in different environment and material conditions.

Downloaded by [University of Michigan-Flint] at 09:31 23 October 2017

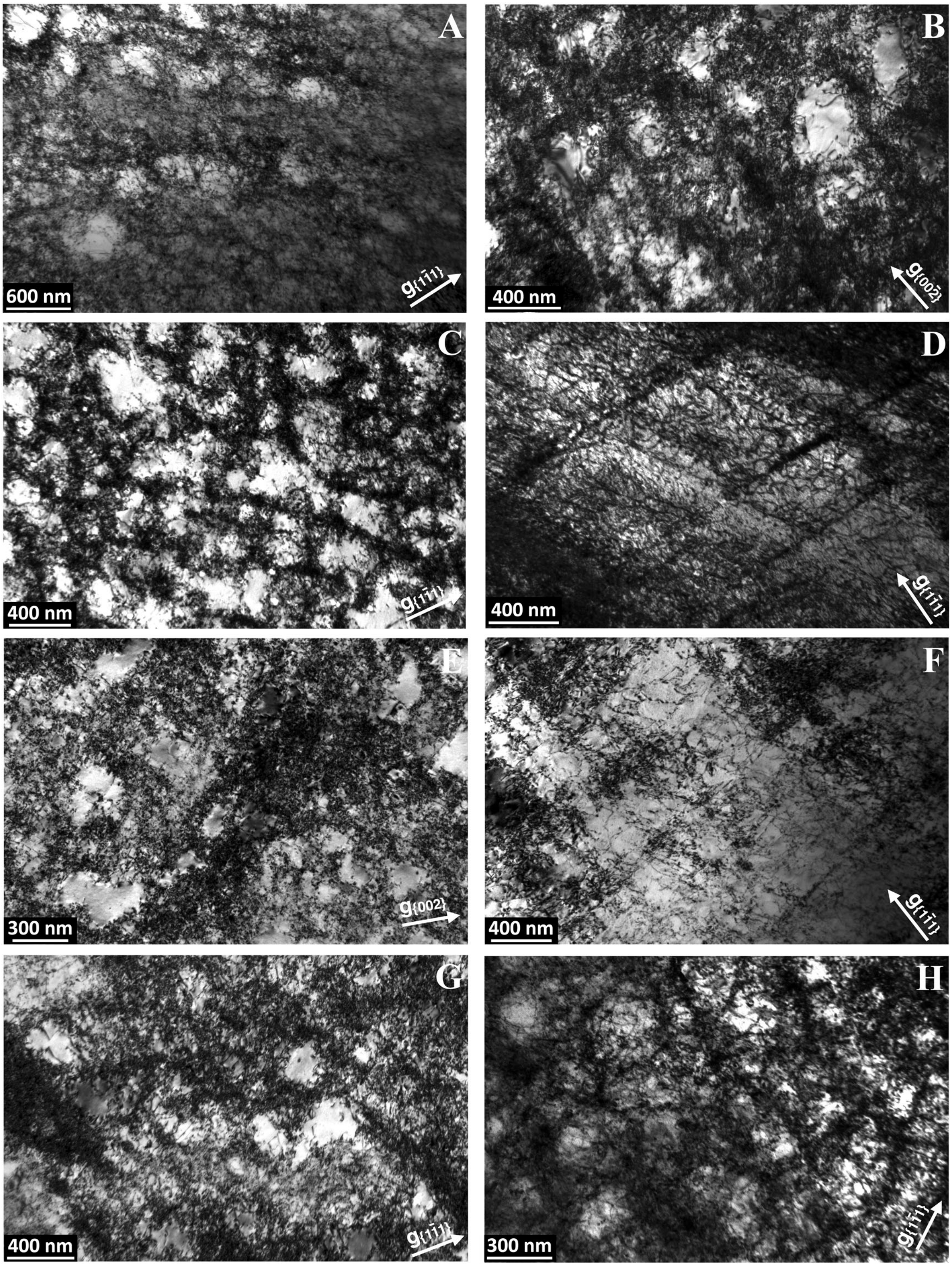

Figure 16. Bright-field 2-beam dynamical micrographs of the TEM samples prepared from tested samples.

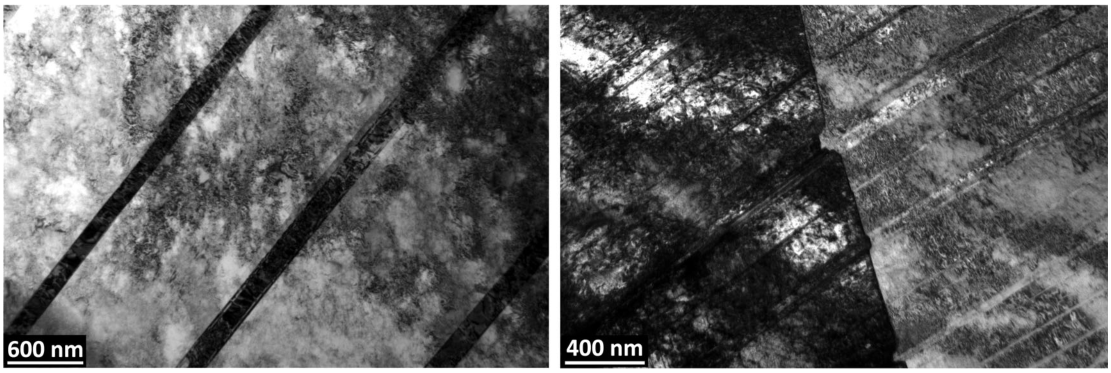

Figure 17. Bright-field images of the deformation bands observed in the TEM samples.

Downloaded by [University of Michigan-Flint] at 09:31 23 October 2017

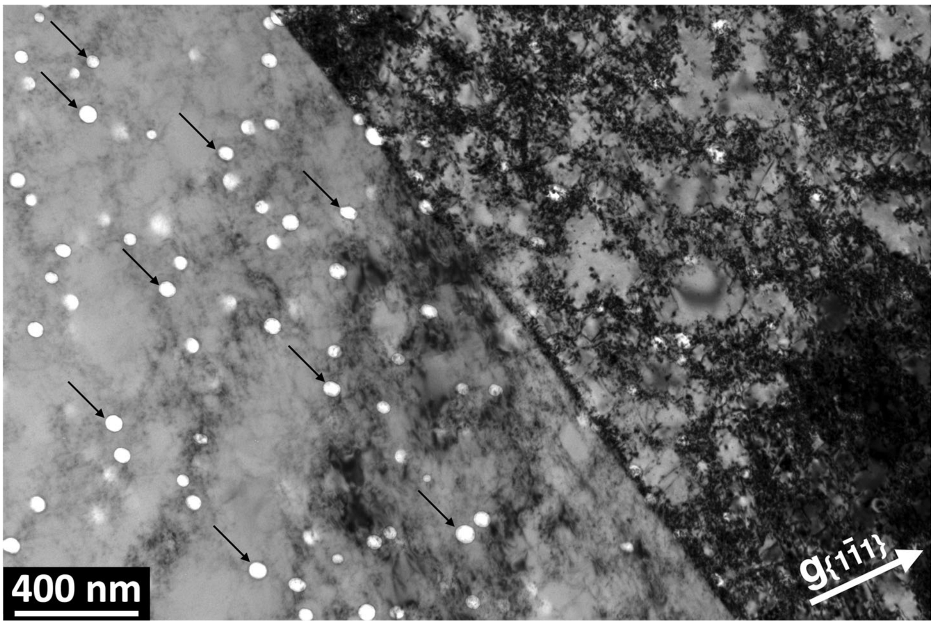

Figure 18. Grain boundary underfocus (∼1 µm) bright-field 2-beam dynamical micrograph (right) of the TEM sample prepared from the tested sample in HTW that contained 1000 appm and was heat treated at 1000°C. The black arrows point at some of the He bubbles (left) in a grain at kinematical conditions.

The PIA samples also showed well developed dislocation cell structures (Figure 16(C,E)). The implantation damage above ≥750°C was completely recovered and the He bubbles were insufficient to produce a significant change in deformation structures (Figure 18). According to Holt [38], a requirement for 3D cell formation is high cross slip ability. A reduction of the dislocation cross slip ability, e.g. due to the black dots, can enhance the formation of localised planar deformation bands and preventing the formation of 3D dislocation cell structures. Thus, it is expected to have more localised deformation in the He as-implanted samples. In fact, more deformation bands, mainly slip bands, were produced in such samples. This is consistent with the change of deformation microstructure which might be a precursor for IASCC. Jiao and Was in [39] have shown that IASCC susceptibility is more correlated to the degree of localised deformation than other parameters like stacking fault energy, hardening or radiation-induced segregation. In the present study, the degree of localised deformation induced by the He bubbles and the He implantation damage is not enough to change substantially the deformation mode, hence higher radiation damage might be needed in order to produce IASCC.

Conclusions and outlook

Homogenised He implantation at 300°C up to 1000 appm in SA, CW and PIA (≤1000°C) conditions does not induce intergranular (IA)SCC initiation in HTW with 2.2 ppm dissolved hydrogen at 288°C in accelerated SSRT with smooth tensile samples. However, the mechanically dominated short-term SSRT may be too short to exclude SCC initiation and could oversee other more time-consuming (e.g. corrosion-dominated) precursor and initiation processes.

This might be related to the absence of a well-marked deformation mode change between the non-implanted and the implanted materials. The number of dislocation channels in the irradiated samples and the He enrichment on the grain boundaries is insufficient to induce IASCC in these conditions. Indeed, the boundary coverage with He bubbles is probably too low (<10%) to significantly reduce the grain boundary strength with respect to the matrix strength.

Our data suggest that a He concentration ≤1000 appm alone cannot induce IASCC, therefore there has to be some synergy between irradiation damage and He. The formation of irradiation-induced dislocation channels (≥0.1 dpa) with high stress concentration on grain boundaries, together with higher He bubbles grain boundary coverage (>10%), could promote intergranular cracking. Future tests thus should include samples with higher irradiation damage (>1 dpa) and similar He contents (e.g. produced by simultaneous He implantation and ion irradiation or irradiation in a spallation neutron source). At the present stage, acceleration of IASCC crack growth in pre-cracked samples by He implantation cannot be excluded and hence, should also be evaluated.

Disclosure statement

No potential conflict of interest was reported by the authors.

Funding

This work was supported by swissnuclear and Euratom research and training programme 2014–2018 under Grant Agreement N° 661913.

ORCID

Ignasi Villacampa http://orcid.org/0000-0002-6039-4588

References

[1] Fukuya K, Shima S, Kazano H, et al. Stress corrosion cracking and intergranular corrosion of neutron irradiated austenitic stainless steels. J Nucl Mater. 1992;191–194:1007–1011.

[2] Jenssen A, Ljungberg L. Irradiation assisted stress corrosion cracking of stainless alloys in BWR normal water chemistry and hydrogen water chemistry. Proceedings of the 6th International Symposium on Environmental Degradation of Materials in

Downloaded by [University of Michigan-Flint] at 09:31 23 October 2017

Nuclear Power Systems – Water Reactors; 1993 Aug 1–5; San Diego, CA, USA.

[3] Garner F, Toloczko M. Irradiation creep and void swelling of austenitic stainless steels at low displacement rates in light water energy systems. J Nucl Mater. 1997;251:252–261.

[4] Sakaguchi N, Watanabe S, Takahashi H, et al. A multi-scale approach to radiation-induced segregation. J Nucl Mater. 2004;329–333:1166–1169.

[5] Was G, Andresen P. The nature of SCC in irradiated stainless steels and nickel-base alloys in LWRs. 17th International Corrosion Congress: Corrosion Control in the Service of Society; 2008 Oct 6–10; Las Vegas, NV, USA.

[6] Bruemmer S, Simonen E, Scott P, et al. Radiation-induced material changes and susceptibility to intergranular failure of light-water-reactor core internals. J Nucl Mater. 1999;274:299–314.

[7] Bruemmer S, Arey B, Charlot L. Grain boundary chromium concentration effects on the IGSCC and IASCC of austenitic stainless steels. International Symposium on Environmental Degradation of Materials in Nuclear Power Systems: Water Reactors (6th); 1993 Aug 3–5; San Diego, CA, USA.

[8] Odette G, Frey D. Development of mechanical property correlation methodology for fusion environments. J Nucl Mater. 1979;85–86:817–822.

[9] Dai Y, Jia X, Chen J, et al. Microstructure of both as-irradiated and deformed 304L stainless steel irradiated with 800 MeV protons. J Nucl Mater. 2001;296:174–182.

[10] Garner F. Radiation damage in austenitic steels. In: Konings RJM, Allen TR, Stoller RE, Yamanaka S, editors. Comprehensive nuclear materials. Vol. 4. Amsterdam: Elsevier Ltd; 2012. p. 33–95.

[11] Fujimoto K, Yonezawa T, Wachi E, et al. Effect of the accelerated irradiation and hydrogen/helium gas on IASCC characteristics for highly irradiated austenitic stainless steels. Proceedings of the 12th International Conference on Environmental Degradation of Materials in Nuclear Power Systems; 2005 Aug 14–18; Salt Lake City, UT, USA.

[12] Ullmaier H, Chen J. Low temperature tensile properties of steels containing high concentration of helium. J Nucl Mater. 2003;318:228–233.

[13] Hasegawa A, Yamamoto N, Shiraishi H. High temperature tensile properties of 316L stainless steel implanted with helium. Mater Trans. 1993;34(11):1090–1096.

[14] Villacampa I, Chen J, Spätig P, et al. Miniaturized flat tensile sample validation for studying the helium effects on IASCC susceptibility. 18th European Corrosion Congress (EUROCORR); 2015 Sep 6–10; Graz, Austria.

[15] Stoller R, Toloczko M, Was G, et al. On the use of SRIM for computing radiation damage exposure. Nucl Instrum Methods B. 2013;310:75–80.

[16] Michalicka J, Hojna A, Keilova E, et al. TEM radiation damage investigation of neutron irradiated baffle-to-former bolt extracted from the decommissioned VVER-440 reactor vessel internals. 16th International Conference on Environmental Degradation of Materials in Nuclear Power Systems – Water Reactors; 2013 Aug 11–15; Asheville, NC, USA.

[17] Greenwood L, Garner F. Hydrogen generation arising from the 59Ni(n,p) reaction and its impact on fission-fusion correlations. J Nucl Mater. 1996;233–237(2):1530–1534.

[18] Seifert H, Ritter S. PSI contribution to the CASTOC Round Robin on EAC of low-alloy RPV steels under BWR conditions. Villigen PSI (CH): Paul Scherrer Institute; 2001. (PSI-Report No.01–08).

[19] Kim Y, Kim Y, Kim D, et al. Effects of hydrogen diffusion on the mechanical properties of austenite 316L at ambient temperature. Mater Trans. 2011;52(3):502–513.

[20] Herms J, Olive J, Puiggali M. Hydrogen embrittlement of 316L type stainless steel. Mater Sci Eng. 1999;272:279–283.

[21] Brozova A, Lynch S. Transgranular stress-corrosion cracking in austenitic stainless steels at high temperatures. In: D Féron, J-M Olive, editors. Corrosion issues in light water reactors: stress corrosion cracking. Amsterdam: Elsevier Ltd; 2007. p. 149–161.

[22] Szost B, Rivera-Diaz-del-Castillo P. Unveiling the nature of hydrogen embrittlement in bearing steels. Scr Mater. 2013;68(7):467–470.

[23] Roychowdhury S, Seifert H, Spätig P, et al. Effect of high-temperature water and hydrogen on the fracture behaviour of a low-alloy reactor pressure vessel steel. J Nucl Mater. 2015;478:343–364.

[24] Odette G, Lucas G. The effects of intermediate temperature irradiation on the mechanical behavior of 300-series austenitic stainless steels. J Nucl Mater. 1991;179–181:572–576.

[25] Chaouadi R, Stergar E, Gavrilov S. Effects of irradiation on the tensile properties and fracture properties of 316L stainless steel. International Light Water Reactors Material Reliability Conference; 2016 Aug 1–4; Chicago, USA.

[26] Robertson JP, Ioda I, Rowcliffe AF, et al. Temperature dependence of the deformation behavior of type 316 stainless steel after low temperature neutron irradiation. In: Nanstad R, Hamilton M, Garner F, Kumar A, editors. Effects of Radiation on Materials: 18th International Symposium; 1996 Jun 25; Hyannis, MA, USA. ASTM STP13896S, West Conshohocken, PA, USA; 1999. p. 671–688.

[27] Elen J, Fenici P. Fast neutron irradiation hardening of austenitic stainless steel at 250°C. J Nucl Mater. 1992;191–194:766–770.

[28] Maloy S, James M, Toloczko M. The high temperature tensile properties on ferritic-martensitic and austenitic steels after irradiation in an 800 MeV proton beam. Conference Proceedings 7th Information Exchange on Actinide and Fission Product Partitioning and Transmutation; 2002 Oct 14–16; Jeju, Republic of Korea, NEA; 2003. p. 669–678.

[29] Bergner F, Pareige C, Hernández-Mayoral M, et al. Application of a three-feature dispersed-barrier hardening model to neutron-irradiated Fe–Cr model alloys. J Nucl Mater. 2014;448(1–3):96–102.

[30] Bement A. Fundamental materials problems in nuclear reactors. Second International Conference on the Strength of Metals and Alloys; 1970 Aug 30–Sep 4; Pacific Grove, CA, USA. p. 693–728.

[31] Tsay K, Maksimkin O, Turubarova L, et al. Microstructural defect evolution in neutron – irradiated 12Cr18Ni9Ti stainless steel during subsequent isochronous annealing. J Nucl Mater. 2013;439(1–3):148–158.

[32] Hashimoto N, Byun T. Deformation-induced martensite formation and dislocation channeling in neutron-irradiated 316 stainless steel. J Nucl Mater. 2007;367–370(B):960–965.

[33] Sauzay M, Bavard K, Karlsen W. TEM observations and finite element modelling of channel deformation in pre-irradiated austenitic stainless steels – interactions with free surfaces and grain boundaries. J Nucl Mater. 2010;406(1):152–165.

[34] Jiao Z, Hesterberg J, Was G. Effect of post-irradiation annealing on hardening, localized deformation and IASCC of a proton-irradiated 304 stainless steel. 17th International Conference on Environmental Degradation of Materials in Nuclear Power Systems – Water Reactors; 2015 Aug 9–13; Ottawa, Ontario, Canada.

[35] Miura T, Fujii K, Fukuya K. Micro-mechanical investigation for effects of helium on grain boundary fracture of austenitic stainless steel. J Nucl Mater. 2015;457:279–290.

[36] Matsuo T, Yamabe J, Matsuoka S. Effects of hydrogen on tensile properties and fracture surface morphologies of type 316L stainless steels. Int J Hydrogen Energ. 2014;39:3542–3551.

[37] Villacampa I, Chen J, Spätig P, et al. Helium effects on 316L austenitic stainless steel fracture mechanism. Key Eng Mater. 2016;713:228–231.

[38] Holt D. Dislocation cell formation in metals. Appl Phys. 1970;41(8):3197–3201.

[39] Jiao Z, Was G. Impact of localized deformation of IASCC in austenitic stainless steels. J Nucl Mater. 2011;408:246–256.